




The Aligned Orbit of the Eccentric Proto Hot Jupiter TOI-3362b*

JUAN I. ESPINOZA-RETAMAL ¹ RAFAEL BRAHM ^{2, 3, 4} CRISTOBAL PETROVICH ^{1, 3} ANDRÉS JORDÁN ^{2, 3, 4, 5}
GUÐMUNDUR STEFÁNSSON ^{6, 7} ELYAR SEDAGHATI ^{8, 2, 3} MELISSA J. HOBSON ^{3, 9} DIEGO J. MUÑOZ ^{2, 3, 4, 10, 11}
GAVIN BOYLE ^{5, 12} RODRIGO LEIVA ^{3, 13} AND VINCENT SUC ^{3, 2, 5}

¹*Instituto de Astrofísica, Pontificia Universidad Católica de Chile, Av. Vicuña Mackenna 4860, 782-0436 Macul, Santiago, Chile*

²*Facultad de Ingeniería y Ciencias, Universidad Adolfo Ibáñez, Av. Diagonal las Torres 2640, Peñalolén, Santiago, Chile*

³*Millennium Institute for Astrophysics, Chile*

⁴*Data Observatory Foundation, Chile*

⁵*El Sauce Observatory – Obstech, Chile*

⁶*NASA Sagan Fellow*

⁷*Department of Astrophysical Sciences, Princeton University, 4 Ivy Lane, Princeton, NJ 08540, USA*

⁸*European Southern Observatory (ESO), Av. Alonso de Córdova 3107, 763 0355 Vitacura, Santiago, Chile*

⁹*Max-Planck-Institut für Astronomie, Königstuhl 17, D-69117 Heidelberg, Germany*

¹⁰*Center for Interdisciplinary Exploration and Research in Astrophysics (CIERA) and Department of Physics and Astronomy, Northwestern University, 2145 Sheridan Road, Evanston, IL 60208, USA*

¹¹*Department of Astronomy and Planetary Science, Northern Arizona University, Flagstaff, AZ 86011, USA*

¹²*Cavendish Laboratory, J J Thomson Avenue, Cambridge, CB3 0HE, UK*

¹³*Instituto de astrofísica de Andalucía, CSIC, Glorieta de la Astronomía s/n, 18008 Granada, Spain*

(Received June 1, 2019; Revised January 10, 2019; Accepted December 1, 2023)

Submitted to ApJL

ABSTRACT

High-eccentricity tidal migration predicts the existence of highly eccentric proto-hot Jupiters on the “tidal circularization track,” meaning that they might eventually become hot Jupiters, but that their migratory journey remains incomplete. Having experienced moderate amounts of tidal evolution of their orbital elements, proto-hot Jupiters systems can be powerful test beds for the underlying mechanisms of eccentricity growth. Notably, they may be used for discriminating between variants of high-eccentricity migration, each predicting a distinct evolution of misalignment between the star and the planet’s orbit. We constrain the spin-orbit misalignment of the proto-hot Jupiter TOI-3362b with high-precision radial velocity observations using ESPRESSO at VLT. The observations reveal a sky-projected obliquity $\lambda = 1.2^{+2.8}_{-2.7}$ deg and constrain the orbital eccentricity to $e = 0.720 \pm 0.016$, making it one of the most eccentric gas giants for which the obliquity has been measured. Although the large eccentricity and the striking orbit alignment of the planet are puzzling, we suggest that ongoing coplanar high-eccentricity migration driven by a distant companion is a possible explanation for the system’s architecture. This distant companion would need to reside beyond 5 au at 95% confidence to be compatible with the available radial velocity observations.

Keywords: Exoplanets (498) — Hot Jupiters (753) — Exoplanet dynamics (490) — Planetary alignment (1243) — Exoplanet migration (2205)

1. INTRODUCTION

Ever since the discovery of 51 Pegasi b (Mayor & Queloz 1995), the existence of hot Jupiters (HJs) has continued to elude a definitive explanation (see Dawson & Johnson (2018) for a review on the possible ori-

Corresponding author: Juan I. Espinoza-Retamal
jiespinzar@uc.cl

* Based on observations made with ESO Telescopes at the La Silla Paranal Observatory under programme ID 110.23Y8.004

gins of HJs). Generally, the theoretical channels proposed to explain these close-in planets fall into two categories. One is high-eccentricity (high- e) tidal migration, in which proto-HJs are first launched into highly eccentric orbits — either through planet-planet scattering (e.g., Rasio & Ford 1996; Beaugé & Nesvorný 2012), von Zeipel-Lidov-Kozai oscillations (e.g., Wu & Murray 2003; Fabrycky & Tremaine 2007; Naoz et al. 2011), or secular interactions (e.g., Wu & Lithwick 2011; Petrovich 2015)— after which tidal friction acts to circularize and shrink the orbits. The other proposed channel posits that HJs acquire their current orbits while still embedded in their parental gas disks, either by in situ formation (e.g., Batygin et al. 2016; Boley et al. 2016) or by formation beyond the ice line, followed by inward migration driven by nebular tides (e.g., Goldreich & Tremaine 1980; Lin & Papaloizou 1986).

If close-in giant planets are indeed the result of high- e tidal migration, we would expect to catch at least some planets on the tidal circularization track (Socrates et al. 2012). Arguably the clearest example of such a system is HD80606b (Naef et al. 2001), which has a distant stellar companion and exhibits extreme orbital eccentricity $e = 0.93$, and high stellar obliquity (Moutou et al. 2009; Pont et al. 2009; Winn et al. 2009; Hébrard et al. 2010), and is thus naturally explained by the von Zeipel-Lidov-Kozai mechanism (Wu & Murray 2003).

Similarly, TOI-3362b, with a reported orbital period $P = 18.1$ days and eccentricity $e = 0.815$ (Dong et al. 2021), may also be considered to be part of the small group of gas giants known to be undergoing high- e tidal migration. Nonetheless, due to the absence of detected (stellar or planetary) companions, coupled with the unresolved matter of stellar obliquity, conclusively identification of the mechanisms that have driven TOI-3362b toward high eccentricity has not been possible to date.

In this Letter, we present further orbital characterization of the TOI-3362b system, obtained from measurements of the Rossiter–McLaughlin (RM) effect and precise long-term RV follow-up observations. Precise in-transit spectroscopic observations with ESPRESSO revealed that the planet’s orbital axis is aligned with the stellar rotation axis with better than three-degree precision and the long-term RV follow-ups obtained with FEROS shows no clear features of long-period companions in the system.

2. OBSERVATIONS

2.1. *Transit Spectroscopy*

We observed a single transit of TOI-3362b with the ESPRESSO spectrograph (Pepe et al. 2021) on the night of the 27th of December 2022, between 04:31 and 08:16

UT. ESPRESSO is the highly-stabilized, fiber-fed cross-dispersed echelle spectrograph installed at the Incoherent Combined Coudé Focus of ESO’s Paranal Observatory in Chile. It covers the wavelength range of 380 to 788 nm at a resolving power of $R \approx 140,000$ in single-UT High-Resolution mode. We obtained 38 spectra of the host star during the primary transit with UT2 at an exposure time of 310 s. The observations were performed under clear sky conditions, with atmospheric seeing in the range of $0.58 - 1.95''$. The spectra have a median S/N of 54 at 550 nm and a median RV uncertainty of 12.4 m/s. The data were reduced with the dedicated data reduction pipeline (v. 2.4.0), including all standard reduction steps, which also provides RVs by fitting a Gaussian model to the calculated cross-correlation function (CCF). The CCF is calculated at steps of 0.5 km/s (representing the sampling of the spectrograph) for ± 100 km/s centered on the estimated systemic velocity. The RM component of the RVs is presented in Figure 1.

2.2. *Photometry*

2.2.1. *Observatoire Moana*

Simultaneously with ESPRESSO observations, we observed the transit using the station of the Observatoire Moana located in El Sauce (ES) Observatory in Chile. This station consists of a 0.6 m CDK robotic telescope coupled to an Andor iKon-L 936 deep depletion $2k \times 2k$ CCD with a scale of $0.67''$ per pixel. We used a Sloan r' filter, and the exposure time was 14 s. The drift of the stars in the CCD during the sequence was smaller than 5 pixels, and the airmass ranged from 1.8 to 1.2. We processed the data with a dedicated pipeline that automatically performs the CCD reduction steps, followed by the measurement of the aperture photometry for the brightest stars in the field. The pipeline also generates the differential light curve of the target star by identifying the optimal comparison stars based on color, brightness, and proximity to the target. The light curve data is displayed in Figure 2 along with the optimal model.

2.2.2. *TESS*

TOI-3362 was observed by the Transiting Exoplanet Survey Satellite (TESS, Ricker et al. 2015) in Sectors 9 and 10 (Year 1) at a cadence of 30 minutes, in Sectors 36 and 37 (Year 3) at a cadence of 10 minutes, and in Sectors 63 and 64 (Year 5) at a cadence of 2 minutes. We searched and downloaded all the light curves using `lightkurve` (Lightkurve Collaboration et al. 2018). TESS light curves were processed by the Science Processing Operations Center (SPOC)

pipeline (Jenkins et al. 2016). The Presearch Data Conditioning (PDC) component of the SPOC pipeline corrects the light curves for pointing or focus-related instrumental signatures, discontinuities resulting from radiation events in the CCD detectors, outliers, and flux contamination. TESS data is displayed in Figure 2 along with the best-fit transit model.

2.2.3. Archival Observations

For this work, we also made use of the ground-based light curves published in Dong et al. (2021), who presented 4 photometric transit observations. Two of them were taken with the Antarctica Search for Transiting Exoplanets (ASTEP) program (Guillot et al. 2015; Mékarinia et al. 2016), which observed the transits of TOI-3362b on the nights of 10th August 2020 and 28th August 2020. This 0.4 m telescope is equipped with an FLI Proline science camera with a KAF-16801E, 4096×4096 front-illuminated CCD with a scale of $0.93''$ per pixel, and it is located on the east Antarctic plateau. Observations were performed in a band that is similar to the R_c in transmission. Also, they observed one transit of TOI-3362b with the 1.0 m telescope at the Las Cumbres Observatory Global Telescope (LCOGT, Brown et al. 2013) Siding Spring Observatory (SSO) node in New South Wales, Australia. This telescope is equipped with a 4096×4096 Sinistro camera with a scale of $0.389''$ per pixel. The transit was observed with the Pan-STARSS z -short and Bessell B filters on the night of 7th February 2021.

2.3. Spectroscopy

2.3.1. FEROS

We obtained 7 spectra of TOI-3362 with FEROS (Kaufer et al. 1999) between 23rd November 2021 and 6th June 2023. FEROS is an echelle spectrograph mounted at the MPG/ESO 2.2 m telescope located at La Silla Observatory, Chile. These observations were performed to identify long-period companions to TOI-3362b. The exposure times were set to 300 s, yielding an average S/N per spectral resolution element of 65. FEROS spectra were reduced, extracted, and analyzed with the *ceres* pipeline (Brahm et al. 2017a). The obtained FEROS RVs are displayed in Figure 3. No signatures of additional planets are identified from these observations.

2.3.2. Archival Observations

For this work, we also made use of the radial velocities published in Dong et al. (2021). The first dataset was obtained from the analysis of 21 spectra taken with the CHIRON echelle spectrograph (Tokovinin et al. 2013)

mounted on the SMARTS 1.5 m telescope at Cerro Tololo in Chile. These observations were made between 15th April 2021 and 12th May 2021. The second dataset was obtained from the analysis of 9 spectra taken with the Minerva-Australis array (Addison et al. 2019). Minerva-Australis is an array of four identical 0.7 m telescopes linked via fiber feeds to a single KiwiSpec echelle spectrograph on Mt. Kent Observatory, Australia. These observations were made between 16th May 2021 and 30th May 2021.

3. STELLAR PARAMETERS

We obtained the stellar parameters by following the procedure presented in Brahm et al. (2019). We use a two-step iterative process. The first process consists of obtaining the atmospheric parameters (T_{eff} , $\log g$, $[\text{Fe}/\text{H}]$, and $v \sin i$) of the host star from a high-resolution spectrum using the *zaspe* code (Brahm et al. 2017b). This code compares the observed spectrum to a grid of synthetic spectra and determines reliable uncertainties that take into account systematic mismatches between the observations and the imperfect theoretical models. For this analysis, we used the co-added out-of-transit ESPRESSO spectra to obtain the atmospheric parameters. The second step consists of obtaining the physical parameters of the star by using publicly available broad-band magnitudes of the star and comparing them with those produced by different PARSEC stellar evolutionary models (Bressan et al. 2012) by taking into account the distance to the star computed from Gaia DR2 (Gaia Collaboration et al. 2018) parallax. This procedure delivers a new value of $\log g$ that is held fixed in a new run of *zaspe*. We iterate between the two procedures until reaching convergence in the $\log g$. The obtained parameters are presented in Table 1.

4. PHOTOMETRIC ANALYSIS

To update the orbital ephemeris of TOI-3362b and look for Transit Timing Variations (TTVs), we modeled all the photometric data presented in Section 2.2 using the *juliet* code (Espinoza et al. 2019). *juliet* uses *batman* (Kreidberg 2015) for the transit model and the *dynesty* dynamic nested sampler (Speagle 2020) to perform bayesian analysis and explore the likelihood space to obtain posterior probability distributions. We placed uninformative priors on the transit parameters R_p/R_* and b , with an informative prior on the stellar density, that was constrained in Section 3. We sampled the limb darkening parameters using the quadratic q_1 and q_2 from Kipping (2013a) with uniform priors. We placed Gaussian priors for each transit mid-point based on the expected values calculated from the orbital period and t_0

Table 1. Stellar properties^a of TOI-3362.

Parameter	Value	Reference
RA ... (J2015.5)	10h23m56.19s	Gaia DR2
Dec ... (J2015.5)	-56d50m35.22s	Gaia DR2
pm ^{RA} (mas/yr)	-24.12 ± 0.05	Gaia DR2
pm ^{DEC} (mas/yr)	7.72 ± 0.05	Gaia DR2
π (mas)	2.79 ± 0.01	Gaia DR2
T (mag)	10.382 ± 0.006	TICv8
B (mag)	11.643 ± 0.12	APASS ^b
V (mag)	10.86 ± 0.010	APASS
G (mag)	10.7051 ± 0.002	Gaia DR2 ^c
G _{BP} (mag)	10.948 ± 0.005	Gaia DR2
G _{RP} (mag)	10.335 ± 0.003	Gaia DR2
J (mag)	9.94 ± 0.02	2MASS ^d
H (mag)	9.72 ± 0.02	2MASS
K _s (mag)	9.69 ± 0.02	2MASS
T_{eff} (K)	6800 ± 100	This work
log g (dex)	4.14 ± 0.01	This work
[Fe/H] ... (dex)	0.24 ± 0.05	This work
$v \sin i$... (km/s)	21.9 ± 0.8	This work
M_{\star} (M_{\odot})	1.53 ± 0.02	This work
R_{\star} (R_{\odot})	1.75 ± 0.02	This work
L_{\star} (L_{\odot})	5.9 ± 0.3	This work
A_V (mag)	0.26 ± 0.06	This work
Age (Gyr)	1.3 ± 0.2	This work
ρ_{\star} (g/cm^3)	0.40 ± 0.02	This work

NOTE—^a The stellar parameters computed in this work do not consider possible systematic differences among different stellar evolutionary models (Tayar et al. 2022) and have underestimated uncertainties, ^bMunari et al. (2014), ^cGaia Collaboration et al. (2018), ^dSkrutskie et al. (2006)

from Dong et al. (2021), with uncertainties of 0.1 days. To account for variability in TESS light curves, we included a Matern-3/2 Gaussian Process (GP) as implemented in *celerite* (Foreman-Mackey et al. 2017) and available in *juliet*. Year 1, 3, and 5 had their own GP kernels to account for differences in variability captured in different epochs and cadences. From this analysis, we ruled out the presence of TTVs greater than ~ 5 minutes and we obtained improved orbital ephemeris of TOI-3362b.

5. JOINT FIT

To precisely constrain the parameters of TOI-3362b and its orbit, we jointly modeled all observations presented in Section 2. In total, our model considered 38 parameters, 10 physical and 28 instrumental (see Table 2). We used *batman* (Kreidberg 2015) to model all the light curves. To reduce the computational cost, we only considered the detrended TESS lightcurve in phases between 0.48 and 0.52 (~ 5 times the transit duration, see Figure 2). For the limb darkening, we considered a quadratic law using the parametrization from Kipping (2013a). To model the out-of-transit radial velocities and RM effect, we used the *rmfit* package (Stefansson et al. 2020, 2022), which uses the framework from Hirano et al. (2010) to model the anomalous RVs seen during the RM effect and *radvel* (Fulton et al. 2018) to model the Keplerian out-of-transit RV curve. We removed one FEROS and two CHIRON measurements that were taken during the transits of the planet, and we did not use them during the analysis. To account for the instrumentation offsets and systematics, we included independent RV offsets and log-uniform jitter terms for each instrument.

We placed uninformative priors for almost all parameters, except for the orbital period and time of mid-transit, which had been constrained in Section 4, and for the stellar density that was constrained in Section 3. Likewise, for β , which is the total line width accounting for both instrumental resolution and macroturbulence velocity. We considered an instrumental broadening of 2.15 km/s because of the ESPRESSO resolution, and following Albrecht et al. (2012) we used the macroturbulence law for hot stars from Gray (1984), which yields a broadening of ~ 7.5 km/s for $T_{eff} \sim 6,800$ K. We added those broadening values in quadrature to set our prior for β , with an uncertainty of 2 km/s. We also tested with an uninformative prior, which resulted in the same posterior values, demonstrating that the posteriors are insensitive to β . All priors and resulting posteriors are shown in Table 2. To estimate the bayesian posteriors and evidences of our model, we used the *dynesty* dynamic nested sampler. Since the number of parameters was 38, we considered 3,500 live points to ensure convergence. Figure 6 shows the joint posterior distributions and histograms for the physical parameters of our model. All parameters appear well-behaved and approximately Gaussian in distribution.

We performed a series of tests to verify our results. First, we tried *emcee* (Foreman-Mackey et al. 2013) to sample the posteriors. Second, we performed a joint fit of the photometry and the out-of-transit RVs with *juliet*. Finally, we carried out a fully independent analysis using the *exoplanet* (Foreman-Mackey et al. 2021)

Table 2. Summary of priors and resulting posteriors of the joint fit.

Parameter	Description	Prior	Posterior
λ	Sky-projected obliquity (deg)	$U(-180, 180)$	$1.2^{+2.8}_{-2.7}$
$v \sin i$	Projected rotational velocity (km/s)	$U(0, 30)$	$20.2^{+1.7}_{-1.6}$
P	Orbital period (days)	$N(18.095368, 0.000012)$	$18.095367^{+0.000008}_{-0.000008}$
t_0	Transit midpoint (BJD)	$N(2458529.3277, 0.00007)$	$2458529.3279^{+0.00006}_{-0.00006}$
ρ_*	Stellar density (g/cm ³)	$N(0.40, 0.02)$	$0.40^{+0.02}_{-0.02}$
b	Impact parameter	$U(0, 1)$	$0.57^{+0.04}_{-0.05}$
R_p/R_*	Radius ratio	$U(0, 1)$	$0.070^{+0.001}_{-0.001}$
e	Eccentricity	$U(0, 0.95)$	$0.720^{+0.016}_{-0.016}$
ω	Argument of periastron (deg)	$U(0, 360)$	$60.6^{+8.0}_{-7.1}$
K	RV semiamplitude (m/s)	$U(0, 1000)$	338^{+27}_{-27}
a/R_*	Scaled semimajor axis	-	$19.1^{+0.3}_{-0.3}$
i	Orbital inclination (deg)	-	$84.25^{+0.34}_{-0.31}$
a	Semimajor axis (au)	-	$0.155^{+0.003}_{-0.003}$
R_p	Planet radius (R_J)	-	$1.2^{+0.02}_{-0.02}$
M_p	Planet mass (M_J)	-	$4.0^{+0.4}_{-0.4}$
ρ_p	Planet mean density (g/cm ³)	-	$3.0^{+0.3}_{-0.3}$
q_1^{ESPRESSO}	ESPRESSO linear limb darkening parameter	$U(0, 1)$	$0.42^{+0.22}_{-0.17}$
q_2^{ESPRESSO}	ESPRESSO quadratic limb darkening parameter	$U(0, 1)$	$0.58^{+0.29}_{-0.34}$
β	Intrinsic stellar line width (km/s)	$N(7.8, 2.0)$	$7.6^{+1.9}_{-1.9}$
γ^{ESPRESSO}	ESPRESSO RV offset (m/s)	$U(7500, 8000)$	7637^{+35}_{-33}
γ^{CHIRON}	CHIRON RV offset (m/s)	$U(6200, 6600)$	6443^{+35}_{-35}
γ^{MINERVA}	Minerva-Australis RV offset (m/s)	$U(7400, 7800)$	7604^{+55}_{-56}
γ^{FEROS}	FEROS RV offset (m/s)	$U(7800, 8200)$	8029^{+35}_{-35}
σ^{ESPRESSO}	ESPRESSO RV jitter (m/s)	$LU(10^{-3}, 100)$	$0.1^{+1.0}_{-0.1}$
σ^{CHIRON}	CHIRON RV jitter (m/s)	$LU(10^{-3}, 100)$	$0.3^{+15.6}_{-0.3}$
σ^{MINERVA}	Minerva-Australis RV jitter (m/s)	$LU(10^{-3}, 100)$	$0.4^{+13.2}_{-0.3}$
σ^{FEROS}	FEROS RV jitter (m/s)	$LU(10^{-3}, 100)$	$0.2^{+7.2}_{-0.2}$
q_1^{TESS}	TESS linear limb darkening parameter	$U(0, 1)$	$0.08^{+0.10}_{-0.05}$
q_2^{TESS}	TESS quadratic limb darkening parameter	$U(0, 1)$	$0.38^{+0.37}_{-0.27}$
$q_1^{r'}$	r' linear limb darkening parameter	$U(0, 1)$	$0.73^{+0.19}_{-0.26}$
$q_2^{r'}$	r' quadratic limb darkening parameter	$U(0, 1)$	$0.72^{+0.20}_{-0.33}$
q_1^B	B linear limb darkening parameter	$U(0, 1)$	$0.05^{+0.10}_{-0.04}$
q_2^B	B quadratic limb darkening parameter	$U(0, 1)$	$0.37^{+0.37}_{-0.27}$
$q_1^{z_s}$	z_s linear limb darkening parameter	$U(0, 1)$	$0.12^{+0.15}_{-0.08}$
$q_2^{z_s}$	z_s quadratic limb darkening parameter	$U(0, 1)$	$0.30^{+0.35}_{-0.22}$
$q_1^{R_c}$	R_c linear limb darkening parameter	$U(0, 1)$	$0.08^{+0.12}_{-0.06}$
$q_2^{R_c}$	R_c quadratic limb darkening parameter	$U(0, 1)$	$0.32^{+0.37}_{-0.23}$
$\sigma_{\text{TESS}}^{\text{Y1}}$	TESS Year 1 photometric jitter	$LU(10^{-6}, 50)$	$0.00142^{+0.00014}_{-0.00012}$
$\sigma_{\text{TESS}}^{\text{Y3}}$	TESS Year 3 photometric jitter	$LU(10^{-6}, 50)$	$0.00089^{+0.00006}_{-0.00006}$
$\sigma_{\text{TESS}}^{\text{Y5}}$	TESS Year 5 photometric jitter	$LU(10^{-6}, 50)$	$0.00002^{+0.00010}_{-0.00001}$
$\sigma_{r'}$	r' photometric jitter	$LU(10^{-6}, 50)$	$0.00351^{+0.00022}_{-0.00021}$
σ_B	B photometric jitter	$LU(10^{-6}, 50)$	$0.00140^{+0.00011}_{-0.00010}$
σ_{z_s}	z_s photometric jitter	$LU(10^{-6}, 50)$	$0.00063^{+0.00012}_{-0.00013}$
σ_{R_c}	R_c photometric jitter	$LU(10^{-6}, 50)$	$0.00174^{+0.00007}_{-0.00007}$

NOTE— $U(a, b)$ denotes a uniform prior with a start value a and end value b . $N(m, \sigma)$ denotes a normal prior with mean m , and standard deviation σ . $LU(a, b)$ denotes a log-uniform prior with a start value a and end value b .

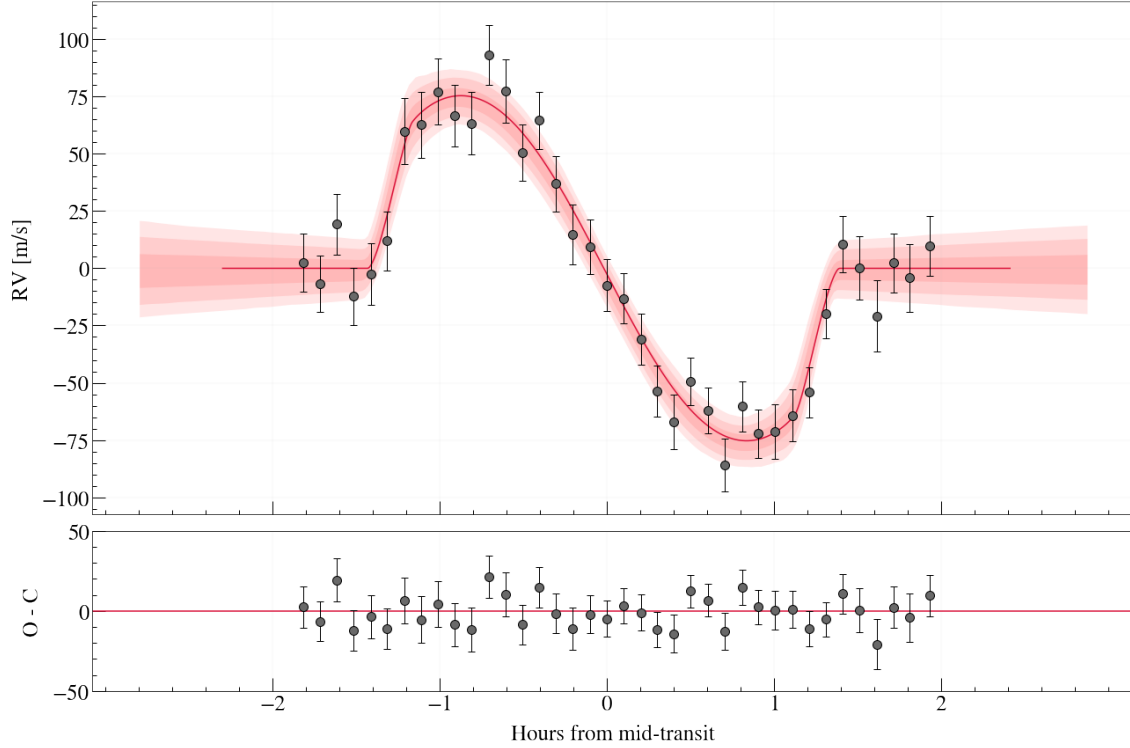


Figure 1. ESPRESSO observations of the RM effect of TOI-3362b with the Keplerian signal removed. The red line shows the best fit, and the red areas show 1, 2, and 3σ models. The bottom panel shows the residuals. The ESPRESSO RVs of this figure without the Keplerian signal removed are available as the Data behind the Figure.

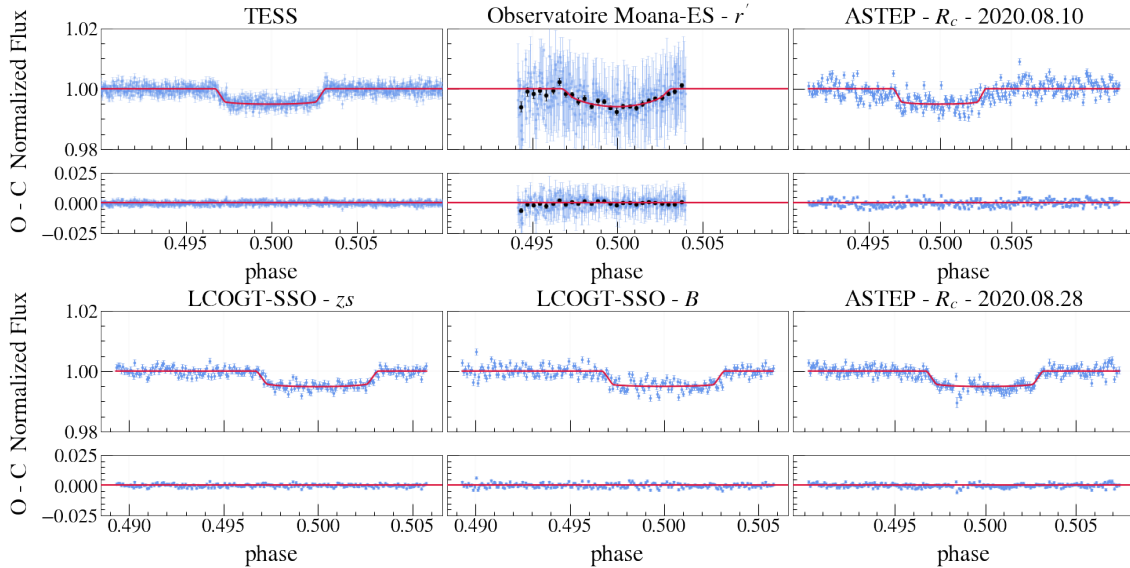


Figure 2. TESS and ground-based transit photometry of TOI-3362b overplotted with best-modeled lightcurves. Residuals are shown for all transits. TESS light curves of different years are shown all together. Observatoire Moana - ES light curve is also shown with 10min-binned data in black, and it is available as the Data behind the Figure.

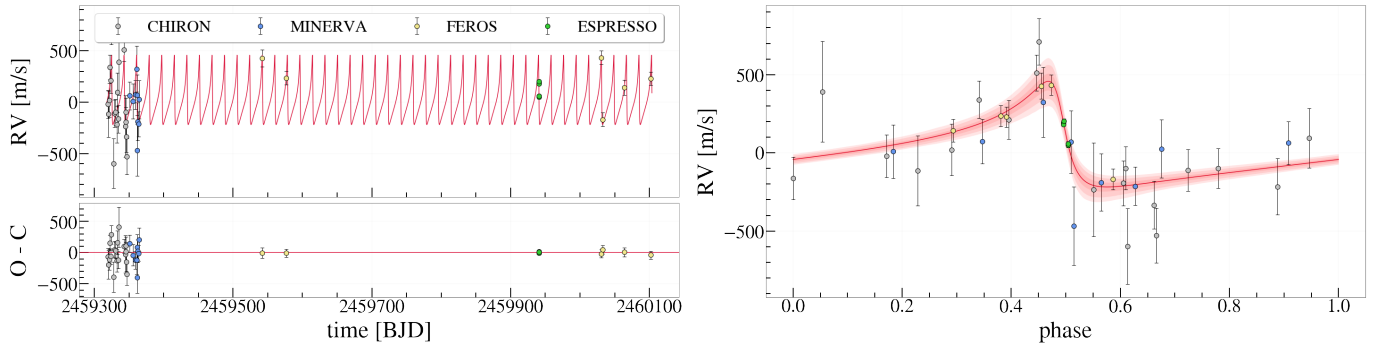


Figure 3. *Left:* Out-of-transit radial velocities of TOI-3362 taken with different instruments. The red curve shows the best model. Residuals are shown at the bottom. *Right:* Out-of-transit radial velocity curve in phase. The red curve shows the best model, and the red regions show 1, 2, and 3σ models. FEROS data is available as the Data behind the Figure.

package implementing the RM effect using the formalism of Hirano et al. (2011). All of them returned a completely consistent set of orbital and stellar obliquity parameters.

Figures 1, 2, and 3 show the different datasets together with the best-fit model. We found a sky-projected obliquity $\lambda = 1.2^{+2.8}_{-2.7}$ deg, which means that the TOI-3362b is perfectly aligned with its host star. This result is surprising given the high eccentricity $e = 0.720 \pm 0.016$ of its orbit. We also found lower values of eccentricity and inclination than the ones reported by Dong et al. (2021) of $0.815^{+0.023}_{-0.032}$ and $89.140^{+0.584}_{-0.668}$ deg, respectively. That is mainly a result of the additional datasets included in this work. In particular, FEROS, ESPRESSO, and TESS Year 5 measurements allowed us to better constrain the orbit of the planet. But in general, the parameters are consistent with the previously reported ones. The baseline of the RV measurements used in this work is ~ 2 years, and residuals show no clear evidence of companions (see Figure 3). Therefore, based on the residuals, we rule out the presence of a companion with at least the same mass in orbits with $a \lesssim 4.5$ au (see Section 6.1).

6. DISCUSSION

The values of the semimajor axis and eccentricity obtained here are consistent with TOI-3362b being a proto HJ undergoing high- e tidal migration. The approximate final orbital separation is $a_{\text{final}} = a(1 - e^2) \approx 9.2 R_{\star}$ or 0.07 au, corresponding to an orbital period of $P_{\text{final}} \approx 6$ days. We estimate a tidal circularization timescale of the planet following Goldreich & Soter (1966):

$$\tau_{\text{circ}} \equiv -\frac{e}{\dot{e}} = \frac{2P}{63\pi} Q'_p \frac{M_p}{M_{\star}} \left(\frac{a}{R_p}\right)^5 F(e), \quad (1)$$

where Q'_p is the planet’s modified tidal quality factor (e.g., Goldreich & Soter 1966; Ogilvie & Lin 2007) and $F(e)$ is an eccentricity-dependent correction factor (Hut

1981). For $e = 0.720$, and assuming pseudo-synchronous rotation of the planet, we have $F(e) \approx 0.004$. Further, assuming that $Q'_p = 10^5 - 10^6$, we have $\tau_{\text{circ}} \sim 0.8 - 8$ Gyr for TOI-3362b. This timescale is longer than that reported by Dong et al. (2021), who inferred $\tau_{\text{circ}} \sim 2.7$ Gyr assuming an eccentricity of 0.815 and $Q'_p = 10^6$. Given that the age of TOI-3362 is 1.3 ± 0.2 Gyr, it is not surprising that we observe the planet in an eccentric orbit. Moreover, the planetary orbit may not have enough time to fully circularize before the host star exits the main sequence. Nevertheless, it could undergo sufficient orbital decay to meet the criteria for classification as an eccentric HJ ($P < 10$ days). Indeed, direct numerical integration¹ shows that the orbit can shrink down to 0.11 au in a timespan of 0.3 – 3 Gyr.

In Figure 4, we compare the orbital properties of TOI-3362b to a larger population of planets, plotting the sky-projected obliquity versus eccentricity for all giant planets with $e > 0.1$. In the left panel, for single-star systems, we can see an emerging trend: sky-projected obliquities tend to be lower with increasing eccentricity. Systems with $0.1 \lesssim e \lesssim 0.4$ are spreading from well-aligned to moderately misaligned ($\lambda \sim 45$ deg). All six systems with $e \gtrsim 0.4$ are well aligned, with TOI-3362b being the most eccentric one and having $\lambda < 10$ deg at a 3σ confidence level thanks to ESPRESSO precision. This trend disappears when we consider binary stars, as shown in the right panel of Figure 4.

6.1. Limits on potential outer companions

The baseline of the RV measurements used in this work is ~ 2 years, and residuals show no clear evidence of companions (see Figure 3). To estimate what kind of planets can produce RV signals consistent with the

¹ We integrate the eccentricity evolution at constant a_{final} , from $e = 0.72$ to $e = 0.53$ at which point the orbit shrunk to 0.11 au or an orbital period of 10 days.

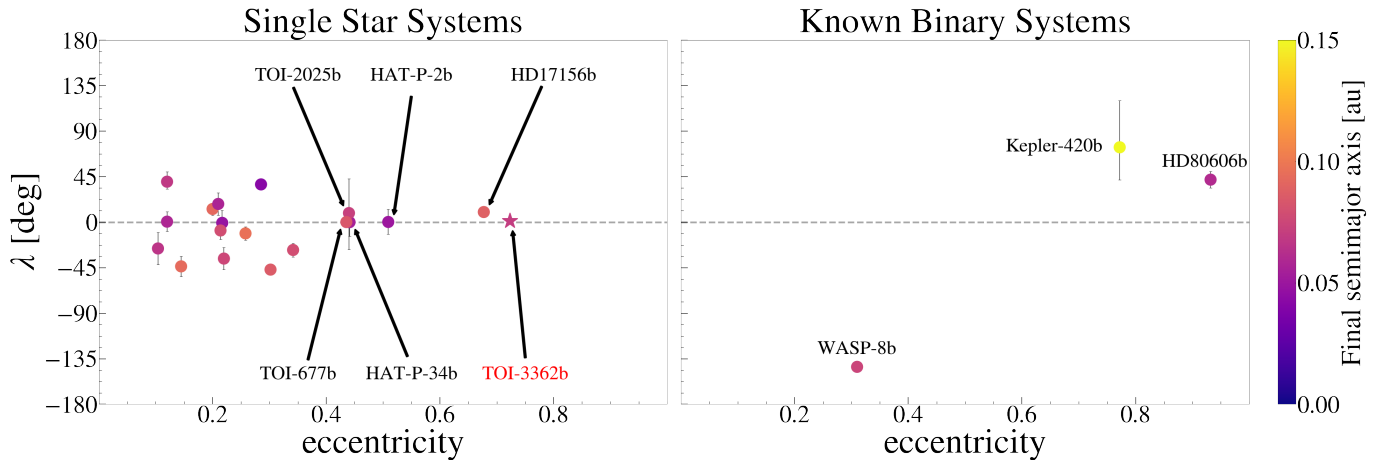


Figure 4. Sky-projected obliquity versus the eccentricity of all giant planets ($M_p > 0.2 M_J$ and $R_p > 8 R_{\oplus}$) with $e > 0.1$ colored by their final semimajor axes $a_{\text{final}} = a(1 - e^2)$ from TEPCat (Southworth 2011). TOI-677b was also measured using ESPRESSO (Sedaghati et al. 2023). The left panel shows single stars, while the right panel shows known binary systems. All planets, excepting Kepler-420b, are or will be hot Jupiters with enough time.

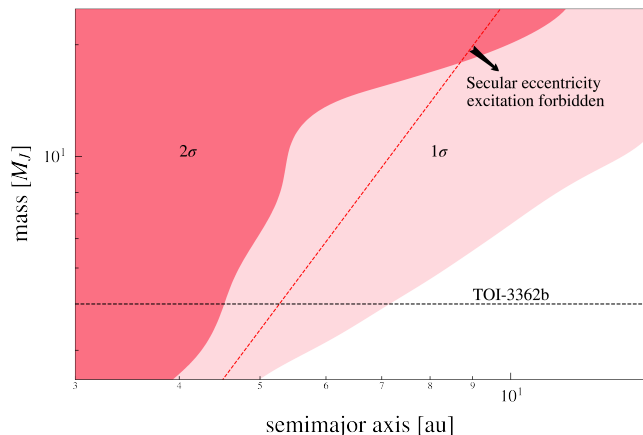


Figure 5. Mass versus semimajor axis diagram for the possible coplanar outer companions to TOI-3362b. Red regions indicate zones where we can rule out the companion at 1 and 2σ confidence levels. The black dashed line shows the mass of TOI-3362b. The line $\epsilon_{\text{gr}} = 1$ (Eq. 2) is shown in red dashed, demarking the regions where secular excitation is quenched by relativistic precession ($\epsilon_{\text{gr}} > 1$). Since the companion might lie in the region where secular eccentricity excitation is forbidden, we discard it as responsible for the current high eccentricity of TOI-3362b.

residuals of the RV model for TOI-3362b, we performed a population synthesis study.

We considered cold Jupiters with masses between 1 and $30 M_J$, and with semimajor axes between 1 and 15 au. The eccentricity of the planets was drawn from a uniform distribution between 0.2 and 0.5, considering that cold Jupiters tend to be moderately eccentric (e.g., Kipping 2013b). The orbital inclinations of the companions were between 0 and 90 deg. With those distributions, we estimated the RV signals of different

companions. Figure 5 shows regions of the mass versus semimajor axis diagram where planets produced RV signals that are inconsistent with the residuals of Figure 3. We discard the existence of similar mass companions to TOI-3362b within ~ 4.5 au (2σ) and ~ 7 au (1σ).

We also estimated the region of the diagram in Figure 5 where secular eccentricity excitation is forbidden by relativistic precession. This occurs when the secular timescale due to the companion is longer than the time scale for relativistic precession. The ratio ϵ_{gr} between these timescales can be calculated as:

$$\epsilon_{\text{gr}} = \frac{GM_{\star}^2 a_c^3 (1 - e_c^2)^{3/2}}{c^2 a^4 M_c}, \quad (2)$$

where a_c , e_c , and M_c are the semimajor axis, eccentricity, and mass of the companion respectively. In Figure 5, the red dashed line corresponds to $\epsilon_{\text{gr}} = 1$ for $e_c = 0.5$.

6.2. Origin

The orbital properties of TOI-3362b and the limits for the presence of an outer companion pose a major challenge to most dynamical paths as we describe next.

- *In-situ formation or disk-driven migration* could naturally explain the small sky-projected obliquity, but does not naturally account for the high eccentricity of the orbit. The mass ratio $M_p/M_{\star} \simeq 2.5 \times 10^{-3}$, may not be large enough to carve a wide and deep enough gap to drive significant eccentricity growth (Papaloizou et al. 2001; Bitsch et al. 2013). If, in turn, the planet resides inside a cavity, simulations show that the eccentricity may grow up to ~ 0.4 (Debras et al. 2021), still well below the planet's eccentricity of 0.72.

- *Planet-planet interactions* at the planet’s current orbital location may have excited the planet’s eccentricity either by scattering or secular excitation (e.g., Anderson & Lai 2017) from a yet undetected companion. Scattering could account for the planetary eccentricity by ejecting planets (e.g., Anderson et al. 2020), though such outcome is not expected to be dominant because the ratio between the planets’ escape velocity and its circular velocity at the current semi-major axis is ~ 1 (Petrovich et al. 2014). An added complication is to retain the small obliquity after scattering. In turn, the secular excitation is largely disfavored by our radial velocity measurements. As shown in Figure 5, our measurements exclude more massive companions inside $\sim 4 - 5$ au (at 2σ), while the potential planet allowed at larger orbital separations would be unable to drive secular excitation as relativistic precession would quench it (red dashed line).
- *Tidal high-eccentricity migration* can naturally account for the planetary eccentricity and semi-major axis. Assuming an equilibrium tide model, the planet would rapidly migrate from ~ 1 au (the circularization timescale from $e = 0.9$ to 0.72 is $\sim 0.15 - 1.5$ Gyr) and would stall as the eccentricity decreases (the circularization timescale from $e = 0.72$ to 0.5 is $\sim 0.3 - 3$ Gyr). The small obliquity disfavors most high-eccentricity migration paths including von Zeipel-Lidov-Kozai oscillations (Fabrycky & Tremaine 2007), planet-planet scattering (Beaugé & Nesvorný 2012), and secular chaos (Wu & Lithwick 2011), while favoring CHEM (Petrovich 2015) that can naturally account for the small obliquity.

In summary, a possible explanation for the system is CHEM driven by a yet undetected massive and distant

companion. If found using longer-term observations, this model would predict that the companion should have a small to moderate mutual inclination ($\lesssim 20$ deg), potentially measurable using upcoming Gaia astrometric data. Using the method² from Espinoza-Retamal et al. (2023) we estimate a probability of $\sim 30\%$ to measure the mutual inclinations if the planet lies at 5 au and use the current RV data. To improve our chances of detecting the potential planet and measuring the mutual inclination through a combined joint RV and Gaia astrometry analysis, long-term radial velocity monitoring will be necessary.

We would like to thank Jiayin Dong for useful discussions on the implementation of the RM effect in **exoplanet**. JIER acknowledges support from the National Agency for Research and Development (ANID) Doctorado Nacional grant 2021-21212378. AJ, RB, CP, and MH acknowledge support from ANID – Millennium Science Initiative – ICN12_009. CP acknowledges support from CATA-Basal AFB-170002, ANID BASAL project FB210003, FONDECYT Regular grant 1210425, CASSACA grant CCJRF2105, and ANID+REC Convocatoria Nacional subvencion a la instalacion en la Academia convocatoria 2020 PAI77200076. RB acknowledges support from FONDECYT project 11200751. AJ acknowledges support from FONDECYT project 1210718. GS acknowledges support provided by NASA through the NASA Hubble Fellowship grant HST-HF2-51519.001-A awarded by the Space Telescope Science Institute, which is operated by the Association of Universities for Research in Astronomy, Inc., for NASA, under contract NAS5-26555.

REFERENCES

- Addison, B., Wright, D. J., Wittenmyer, R. A., et al. 2019, *PASP*, 131, 115003, doi: [10.1088/1538-3873/ab03aa](https://doi.org/10.1088/1538-3873/ab03aa)
- Albrecht, S., Winn, J. N., Johnson, J. A., et al. 2012, *ApJ*, 757, 18, doi: [10.1088/0004-637X/757/1/18](https://doi.org/10.1088/0004-637X/757/1/18)
- Anderson, K. R., & Lai, D. 2017, *MNRAS*, 472, 3692, doi: [10.1093/mnras/stx2250](https://doi.org/10.1093/mnras/stx2250)
- Anderson, K. R., Lai, D., & Pu, B. 2020, *MNRAS*, 491, 1369, doi: [10.1093/mnras/stz3119](https://doi.org/10.1093/mnras/stz3119)
- Batygin, K., Bodenheimer, P. H., & Laughlin, G. P. 2016, *ApJ*, 829, 114, doi: [10.3847/0004-637X/829/2/114](https://doi.org/10.3847/0004-637X/829/2/114)
- Beaugé, C., & Nesvorný, D. 2012, *ApJ*, 751, 119, doi: [10.1088/0004-637X/751/2/119](https://doi.org/10.1088/0004-637X/751/2/119)
- Bitsch, B., Crida, A., Libert, A. S., & Lega, E. 2013, *A&A*, 555, A124, doi: [10.1051/0004-6361/201220310](https://doi.org/10.1051/0004-6361/201220310)

² The method uses the Fisher matrix method to propagate the expected error of Gaia’s astrometric and RV measurements into the parameters of different kinds of possible companions, thus constraining what signals can be detected. The relatively low probability of $\sim 30\%$ comes mostly from the fact that the star is massive and lies at $d \approx 360$ pc, reducing the amplitude of the expected signal as observed by Gaia.

- Boley, A. C., Granados Contreras, A. P., & Gladman, B. 2016, *ApJL*, 817, L17, doi: [10.3847/2041-8205/817/2/L17](https://doi.org/10.3847/2041-8205/817/2/L17)
- Brahm, R., Jordán, A., & Espinoza, N. 2017a, *Publications of the Astronomical Society of the Pacific*, 129, 034002, doi: [10.1088/1538-3873/aa5455](https://doi.org/10.1088/1538-3873/aa5455)
- Brahm, R., Jordán, A., Hartman, J., & Bakos, G. 2017b, *MNRAS*, 467, 971, doi: [10.1093/mnras/stx144](https://doi.org/10.1093/mnras/stx144)
- Brahm, R., Espinoza, N., Jordán, A., et al. 2019, *AJ*, 158, 45, doi: [10.3847/1538-3881/ab279a](https://doi.org/10.3847/1538-3881/ab279a)
- Bressan, A., Marigo, P., Girardi, L., et al. 2012, *MNRAS*, 427, 127, doi: [10.1111/j.1365-2966.2012.21948.x](https://doi.org/10.1111/j.1365-2966.2012.21948.x)
- Brown, T. M., Baliber, N., Bianco, F. B., et al. 2013, *PASP*, 125, 1031, doi: [10.1086/673168](https://doi.org/10.1086/673168)
- Dawson, R. I., & Johnson, J. A. 2018, *ARA&A*, 56, 175, doi: [10.1146/annurev-astro-081817-051853](https://doi.org/10.1146/annurev-astro-081817-051853)
- Debras, F., Baruteau, C., & Donati, J.-F. 2021, *MNRAS*, 500, 1621, doi: [10.1093/mnras/staa3397](https://doi.org/10.1093/mnras/staa3397)
- Dong, J., Huang, C. X., Zhou, G., et al. 2021, *ApJL*, 920, L16, doi: [10.3847/2041-8213/ac2600](https://doi.org/10.3847/2041-8213/ac2600)
- Espinoza, N., Kossakowski, D., & Brahm, R. 2019, *MNRAS*, 490, 2262, doi: [10.1093/mnras/stz2688](https://doi.org/10.1093/mnras/stz2688)
- Espinoza-Retamal, J. I., Zhu, W., & Petrovich, C. 2023, *AJ*, 166, 231, doi: [10.3847/1538-3881/ad00b9](https://doi.org/10.3847/1538-3881/ad00b9)
- Fabrycky, D., & Tremaine, S. 2007, *ApJ*, 669, 1298, doi: [10.1086/521702](https://doi.org/10.1086/521702)
- Foreman-Mackey, D., Agol, E., Ambikasaran, S., & Angus, R. 2017, *AJ*, 154, 220, doi: [10.3847/1538-3881/aa9332](https://doi.org/10.3847/1538-3881/aa9332)
- Foreman-Mackey, D., Hogg, D. W., Lang, D., & Goodman, J. 2013, *PASP*, 125, 306, doi: [10.1086/670067](https://doi.org/10.1086/670067)
- Foreman-Mackey, D., Luger, R., Agol, E., et al. 2021, *The Journal of Open Source Software*, 6, 3285, doi: [10.21105/joss.03285](https://doi.org/10.21105/joss.03285)
- Fulton, B. J., Petigura, E. A., Blunt, S., & Simukoff, E. 2018, *PASP*, 130, 044504, doi: [10.1088/1538-3873/aaaaa8](https://doi.org/10.1088/1538-3873/aaaaa8)
- Gaia Collaboration, Brown, A. G. A., Vallenari, A., et al. 2018, *A&A*, 616, A1, doi: [10.1051/0004-6361/201833051](https://doi.org/10.1051/0004-6361/201833051)
- Goldreich, P., & Soter, S. 1966, *Icarus*, 5, 375, doi: [10.1016/0019-1035\(66\)90051-0](https://doi.org/10.1016/0019-1035(66)90051-0)
- Goldreich, P., & Tremaine, S. 1980, *ApJ*, 241, 425, doi: [10.1086/158356](https://doi.org/10.1086/158356)
- Gray, D. F. 1984, *ApJ*, 281, 719, doi: [10.1086/162149](https://doi.org/10.1086/162149)
- Guillot, T., Abe, L., Agabi, A., et al. 2015, *Astronomische Nachrichten*, 336, 638, doi: [10.1002/asna.201512174](https://doi.org/10.1002/asna.201512174)
- Hébrard, G., Désert, J. M., Díaz, R. F., et al. 2010, *A&A*, 516, A95, doi: [10.1051/0004-6361/201014327](https://doi.org/10.1051/0004-6361/201014327)
- Hirano, T., Suto, Y., Taruya, A., et al. 2010, *ApJ*, 709, 458, doi: [10.1088/0004-637X/709/1/458](https://doi.org/10.1088/0004-637X/709/1/458)
- Hirano, T., Suto, Y., Winn, J. N., et al. 2011, *ApJ*, 742, 69, doi: [10.1088/0004-637X/742/2/69](https://doi.org/10.1088/0004-637X/742/2/69)
- Hut, P. 1981, *A&A*, 99, 126
- Jenkins, J. M., Twicken, J. D., McCauliff, S., et al. 2016, in *Society of Photo-Optical Instrumentation Engineers (SPIE) Conference Series*, Vol. 9913, *Software and Cyberinfrastructure for Astronomy IV*, ed. G. Chiozzi & J. C. Guzman, 99133E, doi: [10.1117/12.2233418](https://doi.org/10.1117/12.2233418)
- Kaufer, A., Stahl, O., Tubbesing, S., et al. 1999, *The Messenger*, 95, 8
- Kipping, D. M. 2013a, *MNRAS*, 435, 2152, doi: [10.1093/mnras/stt1435](https://doi.org/10.1093/mnras/stt1435)
- . 2013b, *MNRAS*, 434, L51, doi: [10.1093/mnrasl/slt075](https://doi.org/10.1093/mnrasl/slt075)
- Kreidberg, L. 2015, *PASP*, 127, 1161, doi: [10.1086/683602](https://doi.org/10.1086/683602)
- Lightkurve Collaboration, Cardoso, J. V. d. M., Hedges, C., et al. 2018, *Lightkurve: Kepler and TESS time series analysis in Python*, *Astrophysics Source Code Library*. <http://ascl.net/1812.013>
- Lin, D. N. C., & Papaloizou, J. 1986, *ApJ*, 309, 846, doi: [10.1086/164653](https://doi.org/10.1086/164653)
- Mayor, M., & Queloz, D. 1995, *Nature*, 378, 355, doi: [10.1038/378355a0](https://doi.org/10.1038/378355a0)
- Mékarnia, D., Guillot, T., Rivet, J. P., et al. 2016, *MNRAS*, 463, 45, doi: [10.1093/mnras/stw1934](https://doi.org/10.1093/mnras/stw1934)
- Moutou, C., Hébrard, G., Bouchy, F., et al. 2009, *A&A*, 498, L5, doi: [10.1051/0004-6361/200911954](https://doi.org/10.1051/0004-6361/200911954)
- Munari, U., Henden, A., Frigo, A., et al. 2014, *AJ*, 148, 81, doi: [10.1088/0004-6256/148/5/81](https://doi.org/10.1088/0004-6256/148/5/81)
- Naef, D., Latham, D. W., Mayor, M., et al. 2001, *A&A*, 375, L27, doi: [10.1051/0004-6361:20010853](https://doi.org/10.1051/0004-6361:20010853)
- Naoz, S., Farr, W. M., Lithwick, Y., Rasio, F. A., & Teyssandier, J. 2011, *Nature*, 473, 187, doi: [10.1038/nature10076](https://doi.org/10.1038/nature10076)
- Ogilvie, G. I., & Lin, D. N. C. 2007, *ApJ*, 661, 1180, doi: [10.1086/515435](https://doi.org/10.1086/515435)
- Papaloizou, J. C. B., Nelson, R. P., & Masset, F. 2001, *A&A*, 366, 263, doi: [10.1051/0004-6361:20000011](https://doi.org/10.1051/0004-6361:20000011)
- Pepe, F., Cristiani, S., Rebolo, R., et al. 2021, *A&A*, 645, A96, doi: [10.1051/0004-6361/202038306](https://doi.org/10.1051/0004-6361/202038306)
- Petrovich, C. 2015, *ApJ*, 805, 75, doi: [10.1088/0004-637X/805/1/75](https://doi.org/10.1088/0004-637X/805/1/75)
- Petrovich, C., Tremaine, S., & Rafikov, R. 2014, *ApJ*, 786, 101, doi: [10.1088/0004-637X/786/2/101](https://doi.org/10.1088/0004-637X/786/2/101)
- Pont, F., Hébrard, G., Irwin, J. M., et al. 2009, *A&A*, 502, 695, doi: [10.1051/0004-6361/200912463](https://doi.org/10.1051/0004-6361/200912463)
- Rasio, F. A., & Ford, E. B. 1996, *Science*, 274, 954, doi: [10.1126/science.274.5289.954](https://doi.org/10.1126/science.274.5289.954)
- Ricker, G. R., Winn, J. N., Vanderspek, R., et al. 2015, *Journal of Astronomical Telescopes, Instruments, and Systems*, 1, 014003, doi: [10.1117/1.JATIS.1.1.014003](https://doi.org/10.1117/1.JATIS.1.1.014003)
- Sedaghati, E., Jordán, A., Brahm, R., et al. 2023, *AJ*, 166, 130, doi: [10.3847/1538-3881/acea84](https://doi.org/10.3847/1538-3881/acea84)

- Skrutskie, M. F., Cutri, R. M., Stiening, R., et al. 2006, *AJ*, 131, 1163, doi: [10.1086/498708](https://doi.org/10.1086/498708)
- Socrates, A., Katz, B., Dong, S., & Tremaine, S. 2012, *ApJ*, 750, 106, doi: [10.1088/0004-637X/750/2/106](https://doi.org/10.1088/0004-637X/750/2/106)
- Southworth, J. 2011, *MNRAS*, 417, 2166, doi: [10.1111/j.1365-2966.2011.19399.x](https://doi.org/10.1111/j.1365-2966.2011.19399.x)
- Speagle, J. S. 2020, *MNRAS*, 493, 3132, doi: [10.1093/mnras/staa278](https://doi.org/10.1093/mnras/staa278)
- Stefansson, G., Mahadevan, S., Maney, M., et al. 2020, *AJ*, 160, 192, doi: [10.3847/1538-3881/abb13a](https://doi.org/10.3847/1538-3881/abb13a)
- Stefansson, G., Mahadevan, S., Petrovich, C., et al. 2022, *ApJL*, 931, L15, doi: [10.3847/2041-8213/ac6e3c](https://doi.org/10.3847/2041-8213/ac6e3c)
- Tayar, J., Claytor, Z. R., Huber, D., & van Saders, J. 2022, *ApJ*, 927, 31, doi: [10.3847/1538-4357/ac4bbc](https://doi.org/10.3847/1538-4357/ac4bbc)
- Tokovinin, A., Fischer, D. A., Bonati, M., et al. 2013, *PASP*, 125, 1336, doi: [10.1086/674012](https://doi.org/10.1086/674012)
- Winn, J. N., Howard, A. W., Johnson, J. A., et al. 2009, *ApJ*, 703, 2091, doi: [10.1088/0004-637X/703/2/2091](https://doi.org/10.1088/0004-637X/703/2/2091)
- Wu, Y., & Lithwick, Y. 2011, *ApJ*, 735, 109, doi: [10.1088/0004-637X/735/2/109](https://doi.org/10.1088/0004-637X/735/2/109)
- Wu, Y., & Murray, N. 2003, *ApJ*, 589, 605, doi: [10.1086/374598](https://doi.org/10.1086/374598)

APPENDIX

A. CORNER PLOT

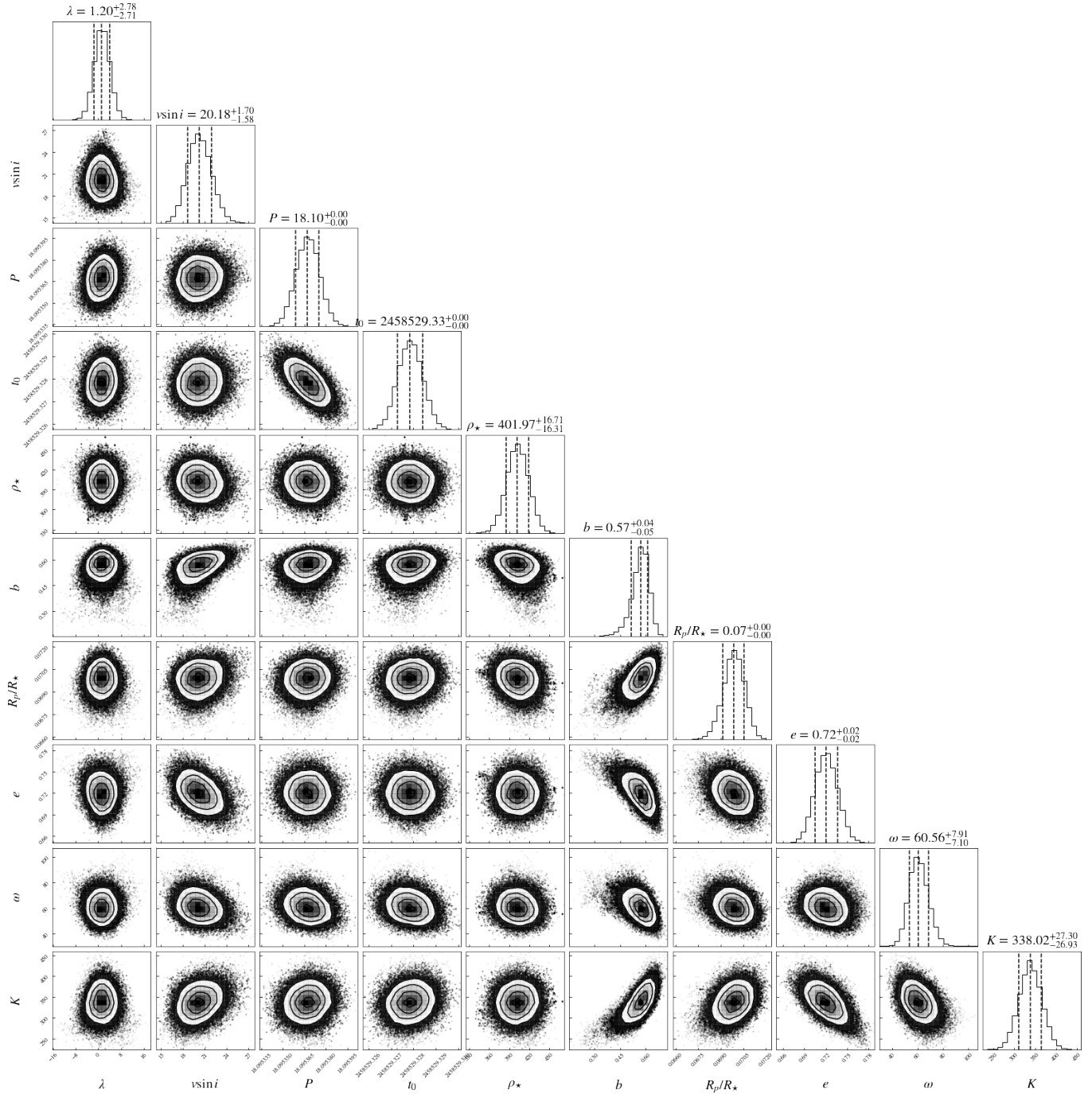


Figure 6. Joint posterior distributions and histograms of the posteriors for the physical parameters of our model.